Monthly Notices of the ROYAL ASTRONOMICAL SOCIETY

MNRAS **512,** 5927–5941 (2022) https://doi.org/10.1093/mnras/stac794
Advance Access publication 2022 March 24

Stress-testing cosmic ray physics: the impact of cosmic rays on the surviving disc of ram-pressure-stripped galaxies

Ryan J. Farber [1]★ Mateusz Ruszkowski,[1] Stephanie Tonnesen[2] and Francisco Holguin [1]

[1] *Department of Astronomy, University of Michigan, 1085 S. University Ave., Ann Arbor, MI 48109, USA*
[2] *Center for Computational Astrophysics, Flatiron Institute, 162 5th Avenue, New York, NY 10010, USA*

Accepted 2022 March 9. Received 2022 March 9; in original form 2021 July 29

ABSTRACT

Cluster spiral galaxies suffer catastrophic losses of the cool, neutral gas component of their interstellar medium due to ram pressure stripping, contributing to the observed quenching of star formation in the disc compared to galaxies in lower density environments. However, the short-term effects of ram pressure on the star formation rate and active galactic nucleus (AGN) activity of galaxies undergoing stripping remain unclear. Numerical studies have recently demonstrated cosmic rays can dramatically influence galaxy evolution for isolated galaxies, yet their influence on ram pressure stripping remains poorly constrained. We perform the first cosmic ray magnetohydrodynamic simulations of an L_* galaxy undergoing ram pressure stripping, including radiative cooling, self-gravity of the gas, star formation, and stellar feedback. We find the microscopic transport of cosmic rays plays a key role in modulating the star formation enhancement experienced by spirals at the outskirts of clusters compared to isolated spirals. Moreover, we find that galaxies undergoing ram pressure stripping exhibit enhanced gas accretion on to their centres, which may explain the prevalence of AGNs in these objects. In agreement with observations, we find cosmic rays significantly boost the global radio emission of cluster spirals. Although the gas removal rate is relatively insensitive to cosmic ray physics, we find that cosmic rays significantly modify the phase distribution of the remaining gas disc. These results suggest observations of galaxies undergoing ram pressure stripping may place novel constraints on cosmic ray calorimetry and transport.

Key words: magnetohydrodynamic – methods: numerical – cosmic rays – galaxies: clusters: intracluster medium – galaxies: evolution – galaxies: star formation.

1 INTRODUCTION

Galaxies exhibit strikingly different properties depending upon the local density of their environment (Dressler 1980). Spirals inhabiting high-density environments such as clusters (cluster spirals) tend to be redder, more anemic in neutral hydrogen gas, have lower star formation rates (SFRs), and stronger magnetic fields than their more isolated counterparts in the field (Hubble & Humason 1931; Butcher & Oemler 1978; Boselli & Gavazzi 2006).

Multiband observations of relatively isolated star-forming spirals orbiting in cluster environments ubiquitously detect copious amounts of multiphase gas pointing away from cluster centre in 'tail' structures extending up to 100 kpc (e.g. in X-rays, Sun et al. 2006, 2009; in Hα, Zhang et al. 2013; in 21-cm emission, Oosterloo & van Gorkom 2005; in CO, Jáchym et al. 2017; Moretti et al. 2018; and see the GASP survey for more examples Poggianti et al. 2017b).

The relative motion between the intracluster medium (ICM) and the galaxy's interstellar medium (ISM) can lead to gas removal from the disc if the ram pressure (RP), $P_{\rm ram} = \rho v^2$, exceeds the gravitational restoring force per unit area, $P_{\rm grav}$ (Gunn & Gott 1972; Roediger 2009). This ram pressure stripping (RPS) should lead to eventual quenching of star formation (e.g. Ignesti et al. 2021) with most of the gas expected to be stripped on the first infall (Jaffé et al. 2015).

However, observations of cluster spirals undergoing RPS can detect moderate *enhancements* of star formation (Vulcani et al. 2018; Roberts & Parker 2020; Roberts et al. 2021, 2022). This star formation enhancement may be related to observations of high-efficiency neutral to molecular gas conversion in RPS galaxies (Moretti et al. 2020a, b), suggesting compression-induced star formation. Moreover, recent observations by the GASP survey suggest the active galactic nucleus (AGN) fraction is strongly enhanced relative to the field (Poggianti et al. 2017a; Radovich et al. 2019; Peluso et al. 2022).

Some hydrodynamical simulations have studied the effect of RP on the surviving gas disc. Schulz & Struck (2001) coined the term 'disc annealing', or the compression of the inner surviving disc via angular momentum transport. Tonnesen & Bryan (2009) found that at low RP strengths, more gas was compressed than removed by the ICM, and Tonnesen (2019) argued that early compression could have a long-lasting impact on the amount of gas that is stripped.

Additional simulations have focused on the impact of RP on the SFR of galaxies, although no consensus has been reached. While many simulations predict that in some cases RP can cause a modest increase in the disc SFR (Kronberger et al. 2008; Steinhauser, Schindler & Springel 2016; Ruggiero & Lima Neto 2017; Lee et al. 2020), some find that the global SFR is suppressed (Tonnesen & Bryan 2012; Roediger et al. 2014; Lee et al. 2020), and others find that in a few cases the SFR can be boosted by a factor of a few (Bekki 2013). These simulations span a range of galaxy masses, RP strengths, and numerical implementations, and therefore cannot yet be combined into a coherent picture.

★ E-mail: rjfarber@umich.edu

© 2022 The Author(s)
Published by Oxford University Press on behalf of Royal Astronomical Society

Downloaded from https://academic.oup.com/mnras/article/512/4/5927/6553836 by Columbia University user on 10 August 2022

A growing body of literature has explored the impact of magnetic fields on ram-pressure-stripped galaxies using numerical simulations. While magnetohydrodynamic (MHD) simulations have shown that draping of a magnetized ICM (Lyutikov 2006; Ruszkowski et al. 2007, 2008; Dursi & Pfrommer 2008; Pfrommer & Dursi 2010; Ruszkowski et al. 2014) helps to reproduce the smooth (as opposed to clumpy) morphology of RPS tails in agreement with recent observations (Müller et al. 2021), they find little impact on the gas stripping rate compared to purely hydrodynamic simulations (Ruszkowski et al. 2014). However, Ruszkowski et al. (2014) find an increase in magnetic pressure along the disc due to draping. Similarly, simulations with disc magnetic fields find little impact on the stripping rate as long as the gas surface density is not impacted (Tonnesen & Stone 2014; Ramos-Martínez, Gómez & Pérez-Villegas 2018). Interestingly, Ramos-Martínez et al. (2018) find magnetized, flared discs act to deflect ICM material towards the galactic centre region.

In contrast, the effect of cosmic rays (CRs) on RPS remains largely unexamined. Bustard et al. (2020) performed simulations including CRs, radiative cooling, and the derived star formation history of the Large Magellanic Cloud. They showed CR-driven galactic winds in combination with RPS can contribute to the Magellanic Stream. To our knowledge, CRs have never been studied for more massive L_* galaxies in a cluster environment. Yet CRs have shown to play a crucial role in the evolution of isolated galaxies (Enßlin et al. 2007; Everett et al. 2008; Uhlig et al. 2012; Booth et al. 2013; Salem & Bryan 2014; Girichidis et al. 2016, 2018; Simpson et al. 2016; Pfrommer et al. 2017a, b; Ruszkowski, Yang & Zweibel 2017; Wiener, Pfrommer & Oh 2017; Butsky & Quinn 2018; Farber et al. 2018; Heintz & Zweibel 2018; Chan et al. 2019; Holguin et al. 2019; Wiener, Zweibel & Ruszkowski 2019; Hopkins et al. 2020, 2021; Ji et al. 2020; Semenov, Kravtsov & Caprioli 2021, see Zweibel 2017 for a review).

Including CRs is essential to understanding the physics underlying observations of RPS galaxies. The non-thermal pressure of CRs tends to produce discs of larger scale height, which should be more easily stripped. Likewise, CR-driven galactic winds tend to be cooler and of higher density than thermal outflows, suggesting more efficient removal of the neutral medium from galaxies. On the other hand, previous work has shown that CRs suppress the SFR in galaxies, as their non-thermal pressure counteracts contraction of gas to star-forming densities. CR models with consequently reduced stellar feedback may exhibit weaker outflows, diminishing the amount of gas that is stripped.

Beyond the dynamics of RPS, CRs are fundamental towards understanding radio continuum observations of RPS galaxies, the measurements of which indicate a global radio excess compared to the far-infrared (FIR) to radio correlation (FRC) (Dickey & Salpeter 1984; Beck & Golla 1988; Yun, Reddy & Condon 2001; Paladino et al. 2006). Since enhanced star formation would boost both the radio and the FIR (Lacki, Thompson & Quataert 2010), previous work suggested magnetic compression by the ICM wind on the leading edge of the galaxy could explain the boosted radio emission (Scodeggio & Gavazzi 1993).

However, Murphy et al. (2009) utilized *Spitzer* FIR and VLA radio continuum imaging to show a *paucity* of radio emission on the leading edge of the galaxy's orbital motion, precisely where one would expect magnetic compression to dominate. Nevertheless, they observe global radio enhancement. The local radio deficits with global radio enhancement was confirmed by Vollmer et al. (2009, 2010, 2013) in Virgo cluster galaxies with multiwaveband measurements. They propose that both the local deficits and global enhancement of radio emission can be explained by variations in the CR electron number density.[1] Although the magnetic field is compressed on the leading edge, CR electrons may be easily stripped and their consequently low density suppresses the radio emission. Meanwhile, shocks driven into the ISM by the interaction with the ICM can re-accelerate CR, boosting the global radio emission. However, Pfrommer & Dursi (2010) suggest magnetic draping can explain the deficits in radio emission.

In this work, we determine the impact of CR and their transport, on properties of galaxies undergoing RPS. The outline of this paper is as follows: In Section 2, we describe the initial conditions, boundary conditions, galaxy model, and numerical methods utilized to perform this work including MHD, CR, radiative cooling, self-gravity of the gas, star formation, and stellar feedback. In Section 3, we present and discuss our results. In Section 3.1, we consider the morphological evolution of the simulations we performed, finding CR crucially modify the outflows in isolated galaxies, yet do not evidently modify the morphology when galaxies undergo RPS. Thus, the stripping rates analysed in Section 3.2 do not show much difference with or without CR. However, in Section 3.3 we find CRs protect low-temperature gas from being stripped, possibly helping to explain observations of molecular gas in RPS tails. CRs dramatically influence star formation, as we show in Section 3.4. Intriguingly, we find in Section 3.5 that CRs modify the accretion rate on to the galactic centre with important implications for observations of AGNs in RPS galaxies. The transport of CRs fundamentally impacts the radio emission, which we discuss in Section 3.6. We indicate limitations of our study and directions for future work in Section 4. Finally, we conclude in Section 5.

2 METHODS

2.1 Numerical techniques

We performed our simulations using the adaptive mesh refinement MHD code FLASH 4.2.2 (Fryxell et al. 2000; Dubey, Reid & Fisher 2008), with the directionally unsplit staggered mesh (USM) solver (Lee & Deane 2009; Lee 2013). The USM is a finite-volume, high-order Godunov scheme that utilizes constrained transport to satisfy the solenoidal constraint of Maxwell's equations to machine precision.

Additionally, we include self-gravity, radiative cooling, star formation, and feedback as source and sink terms in the MHD equations. We include the passive advection of a concentration variable C, used to mark the initial disc gas.[2] We further extend the MHD equations to include CR as a second ultrarelativistic fluid (Yang et al. 2012; Yang, Ruszkowski & Zweibel 2013; Ruszkowski et al. 2017; Yang & Ruszkowski 2017; Holguin et al. 2019); see Farber et al. (2018) for the system of equations we solve.

To include self-gravity of the baryons (gas and stellar population particles[3]), we solve the Poisson equation using the Huang & Greengard (1999) multigrid solver in FLASH (Huang & Greengard 1999; Ricker 2008). The multigrid solver implemented in FLASH extends Huang & Greengard (1999) for compatibility with FLASH's numerical structure, namely, finite volume discretization of the fluid

[1]The radio emission is expected to be produced via synchrotron emission as the CR electrons gyrate along magnetic field lines.
[2]We set C = 1 in the disc and zero elsewhere.
[3]We utilize static potentials to include the gravitational influence of pre-existing stars; stellar population particles form during the simulation runtime.

Downloaded from https://academic.oup.com/mnras/article/512/4/5927/6553836 by Columbia University user on 10 August 2022

equations with shared data on an oct-tree mesh, enabling efficient parallelization. That is, the multigrid method utilizes a direct solver for individual mesh blocks; see Ricker (2008) for further details.

We utilized the hybrid scheme for radiative cooling and heating of Gnedin & Kravtsov (2011). The implementation automatically switches between an explicit and implicit solver depending on the time-step constraint, enabling efficient and accurate treatment of radiative cooling and heating. For the rates, we interpolate to the nearest temperature and density using a table generated with CLOUDY (Ferland et al. 1998) assuming a constant solar metallicity and a constant metagalactic UV background; see e.g. Semenov et al. (2021) for further details.

To accelerate the computations we impose a minimum time-step $\mathrm{dt_{min}} = 10^4$ yr. We do so while maintaining numerical stability by limiting the bulk and generalized sound speeds to

$$v_{\max} \leq C_{\rm cfl} \frac{\Delta x}{\Delta t_{\min}}, \tag{1}$$

where $C_{\rm cfl} = 0.2$ is the Courant–Friedrichs–Lewy number and Δx is the width of a cell.

We impose the speed limit via dissipation of thermal and CR energy such that the generalized sound speed obeys the speed limit $c_s = \sqrt{(\gamma_{\rm th} p_{\rm th} + \gamma_{\rm cr} p_{\rm cr})/\rho}$ and similarly for the bulk speed.[4] Rather than limiting the Alfvén speed directly, we utilize the hybrid Riemann solver implemented in FLASH, as modified to utilize the HLLC Riemann solver in smooth regions and the LLF Riemann solver in shock-detected regions for increased numerical stability (Lee, private communication).

We perform our simulations in a box of dimensions $(-32$ kpc, 32 kpc$)^3$ with the galaxy centred at the origin with the spin axis pointing in the z-direction. We uniformly resolve $|z| < 4$ kpc with seven levels of refinement such that our galactic disc achieves a resolution of 127 pc and resolution degrades away from the galactic disc to a base grid with four levels of refinement and a physical resolution of $\sim$1 kpc.

Note that our box is relatively small to minimize the resolution elements covering $|z| < 4$ kpc; we adopt such a step-wise refinement pattern to avoid 'corners' of different resolution elements, which we found produced spuriously reflected waves and generated unphysical structures in the magnetic field.

We employ diode boundary conditions (modified to prevent inflow while including self-gravity, see Appendix B) on all box faces. For the `FaceOn` and `EdgeOn` runs, after waiting 40 Myr to allow the initial conditions to relax, we inject a wind through the -z and -y boundaries, respectively, following the parameters of Ruszkowski et al. (2014). That is, we model an ICM wind with a density of $n_{\rm wind} = 5 \times 10^{-4}$ cm^{-3}, temperature $T_{\rm wind} = 7 \times 10^7$ K, magnetic field strength of 2 μG perpendicular to the wind, zero along the direction of the wind, and a maximum wind speed of 1300 km s^{-1}. We use an accelerating profile of the wind speed to model the orbital motion of the galaxy falling towards the centre of the cluster (Tonnesen 2019), following the model of Ruszkowski et al. (2014), namely $v_w(t) = f(t) v_{\rm max,\,w}$, where

$$f_{\rm in}(t) = 1 - \begin{cases} 1 - 1.5x^2 + 0.75x^3 & \text{if} x \leq 1 \\ 0.25(2-x)^3 & \text{if} 1 < x < 2 \\ 0 & \text{if} x \geq 2 \end{cases} \tag{2}$$

[4]Note that ensuring $\mathrm{dt_{min}} = 10^4$ yr is equivalent to a ceiling of $\sim 10^4$ km s^{-1} at our best resolution. Since the maximum inflow speed is about 10 times smaller, we do not expect our simulations to be impacted by the bulk speed limiter.

Table 1. Numerical parameters.

Name	Value
$\mathrm{dt_{min}}$	10^4 yr
$C_{\rm cfl}$	0.2
$\rho_{*,\min}$	1 cm^{-3}
$E_{\rm SN}$	10^{51} erg
$f_{\rm th}$	0.717
$f_{\rm cr}$	0.1
$\kappa_{\parallel}$	$3 \cdot 10^{28}$ cm^2 s^{-1}
$\kappa_{\perp}$	0
$M_{*,\rm disk}$	10^{11} M$_\odot$
$M_{*,\rm bulge}$	10^{10} M$_\odot$
$M_{\rm gas,\,disc}$	10^{11} M$_\odot$
$M_{\rm DM,\,core}$	$1.1 \cdot 10^{11}$ M$_\odot$
$r_{0,\,*,\,\rm disc}$	4 kpc
$r_{0,\,\rm gas,\,disc}$	7 kpc
$r_{0,\,*,\,\rm bulge}$	0.4 kpc
$z_{0,\,*,\,\rm disc}$	0.25 kpc
$z_{0,\,\rm gas,\,disc}$	0.4 kpc
$\mathrm{R_{disc}}$	26 kpc
$B_{0,\,\rm x}$	1 μG
a_0	10^3
$\rho_{0,\,\rm CGM}$	9.2×10^{-5} cm^{-3}
$T_{0,\,\rm CGM}$	4.15×10^6 K
$n_{\rm wind}$	5×10^{-4} cm^{-3}
$T_{\rm wind}$	7×10^7 K
$v_{\rm max,\,wind}$	1300 km s^{-1}
$B_{\perp,\,\rm wind,\,1}$	2×10^{-6}G
$B_{\perp,\,\rm wind,\,2}$	2×10^{-6}G
$B_{\parallel,\,\rm wind}$	0
$L_{\rm box}$	64.8 kpc
$\mathrm{dx_{min}}$	127 pc
$\mathrm{dx_{max}}$	1 kpc
$\mathrm{|z|_{dx,\,min}}$	4 kpc

with $x \equiv t/\Delta t$ and $\Delta t \approx 59$ Myr. That is, the wind reaches maximum velocity at 158 Myr (since we delay onset of the wind 40 Myr) and is constant thereafter. See Table 1 for a list of the parameters employed in this study.

2.1.1 *Star formation and feedback*

We employ the star formation and stellar feedback prescriptions used in the ART (Kravtsov 1999; Kravtsov, Klypin & Hoffman 2002; Rudd, Zentner & Kravtsov 2008; Gnedin & Kravtsov 2011) simulations of galaxy evolution (Semenov, Kravtsov & Gnedin 2016, 2017, 2018; Semenov et al. 2021). That is, we permit gas to form stars when the gas density exceeds a critical value $n_{*,\min} = 1$ cm^{-3} with the SFR density ρ_* parametrized to match the Kennicutt–Schmidt relation (Schmidt 1959; Kennicutt 1998):

$$\dot{\rho}_* = \epsilon_{\rm ff} \frac{\rho}{t_{\rm ff}}, \tag{3}$$

where $\epsilon_{\rm ff}$ is the star formation efficiency per free-fall time $t_{\rm ff}$. We set $\epsilon_{\rm ff} = 0.01$ in agreement with observationally inferred low local star formation and long galactic depletion times of star-forming gas (see Krumholz & Tan 2007; Leroy et al. 2017; Semenov et al. 2018).

When the gas density of a cell exceeds the minimum density for star formation we create a stellar population particle with the mass proportional to N, where N is the number of occurrence, drawn from a Poisson distribution, characterized by the expected value $\lambda = \rho_* \mathrm{d}V \mathrm{d}t/m_*$, min. However, we limit the value of N to not exceed $m_{\rm gas}/m_{*,\,\rm min}$, where $m_{*,\,\rm min} = 10^4$ M$_\odot$ is the minimum stellar

Downloaded from https://academic.oup.com/mnras/article/512/4/5927/6553836 by Columbia University user on 10 August 2022

population mass we enforce to avoid creating a computationally intractably large number of particles. We also require the total stellar population particle mass not to exceed 2/3 $m_{\rm gas}$ to avoid consuming all the gas in the cell. Upon creation of the stellar population particle, we remove its mass from the gas in the cell it inhabits.

For 40 Myr immediately succeeding the creation of a stellar population particle we apply feedback from massive stars, modelling proto-stellar jets, massive stellar winds, and radiation pressure, preceding Type II supernovae. We sample our stellar population particles with a Chabrier initial mass function to determine the contribution from massive stars $\gtrsim$8 $M_\odot$. For each massive star we inject 0.1×10^{51} erg as CR energy, as well as thermal energy and momentum according to the subgrid model of Martizzi, Faucher-Giguère & Quataert (2015).

The Martizzi et al. (2015) momentum feedback subgrid model takes into account local conditions and our resolution to inject the appropriate amount of momentum produced during the (unresolved) Sedov–Taylor phase (see also Iffrig & Hennebelle 2015; Kim & Ostriker 2015; Walch & Naab 2015). We boost the injected momentum by a factor of five to account for the unresolved clustering of supernovae (Gentry et al. 2017, 2019), the influence of CR on the supernova momentum deposition (Diesing & Caprioli 2018), and to account for advection errors (Agertz et al. 2013; Semenov et al. 2018).

2.1.2 CR models

We bracket the parameter space of CR transport and calorimetry via three cases: (1) No CR (`NoCR`), i.e. modelling the case of complete calorimetry. (2) CR that simply advect with the thermal gas (`ADV`). This case models unresolved tangled structure of the magnetic field in the galactic disc, preventing CR from escaping into the circumgalactic medium (CGM) or effectively a strong suppression of CR diffusion and cooling near star formation sites (Semenov et al. 2021). (3) CRs anisotropically diffuse along magnetic field lines with a diffusion coefficient parallel to the magnetic field of 3×10^{28} cm^2 s^{-1} and zero perpendicular diffusion (`DIF`). We note that these three cases are meant to bracket the possible results of a more detailed CR transport modelling, which remains highly uncertain (see the dozens of models of Hopkins et al. 2021).[5]

2.2 Galaxy model

We model a massive spiral galaxy with a flat rotation curve $v_{\rm disp} = 200$ km s^{-1}, composed of a gaseous disc, hot halo, stellar disc, stellar bulge, and dark matter halo initially in hydrostatic equilibrium (see Tonnesen & Bryan 2009; Tonnesen & Bryan 2010).

To directly follow Roediger & Brüggen (2006) we use a Plummer–Kuzmin potential for the stellar disc (Miyamoto & Nagai 1975), a Hernquist profile for the stellar bulge (Hernquist 1993), and a Burkert (1995) potential for the dark matter halo[6] (see Table 1 for the masses and scale lengths of each component).

We employ the same magnetic field configuration initial conditions as model TORL of Tonnesen & Stone (2014). Namely, we initialize the magnetic field to be weak in the galactic central region (where the velocity field changes rapidly), peaking in strength a few kpc from the galactic centre, diminishing gradually with increasing galactic radius, and set to zero outside the disc. That is, we employ the following vector potential (with A_z set to a constant outside the disc):

$$A_x = A_y = 0 \tag{4}$$

$$A_z = \sqrt{a_{zf}} e^{-6R_{\rm cyl}} \frac{-6\sin(2.5R_{\rm cyl}) - 2.5\cos(2.5R_{\rm cyl})}{6^2 + 2.5^2} \tag{5}$$

$$a_{zf} = 1000(-|z| + 1)^{80} \tag{6}$$

Note that the cut-off in magnetic field strength at the disc-edge ensures the magnetic pressure is subdominant to the thermal pressure, reducing disc expansion as well as growth of the magnetic field due to shear between the disc and the CGM.

The plasma beta, which is the ratio of thermal to magnetic pressures, $\beta \equiv P_{\rm gas}/P_{\rm mag}$, ranges from 100 to a maximum of $\sim$2 in the disc mid-plane a few kpc from the galactic centre region (see fig. 2 of Tonnesen & Stone 2014). Since the magnetic pressure is subdominant to the thermal pressure the magnetic field does not have a strong effect on the disc. The chosen magnetic field morphology enables easier comparison to our previous work (Tonnesen & Stone 2014) as it is reproducible, reduces variability due to instabilities, and is divergence-free.

3 RESULTS AND DISCUSSION

We begin the presentation of our results in Section 3.1 by graphically illustrating the nine runs we have analysed and indicating their morphological evolution in Figs 1–3. Then we explore the impact of CR on the stripping rates in Section 3.2 and the gas phase distribution in Section 3.3. In Section 3.4, we discuss the impact of CR and their feedback on the SFR in galaxies undergoing RPS at cluster outskirts. We consider the impact of CR on the accretion of gas towards the galactic centre in Section 3.5. See Table 2 for our nomenclature.

3.1 Galactic morphology

In this section, we analyse the morphological evolution of galactic discs. We performed a grid of nine simulations, composed of three CR models and three galaxy models. We performed simulations (a) without CR (`NoCR`), (b) where CR purely advect with the gas (`ADV`), and (c) including the anisotropic diffusion of CR along magnetic field lines (`DIF` see Section 2.1.2 for further details). For each CR model we simulated (i) field galaxies not subject to any ICM wind (`Isolated`), and galaxies falling into a cluster such that the spin axis points (ii) face-on (`FaceOn`) or (iii) orthogonal to (`EdgeOn`) the direction of the orbital motion.

In all cases, the gas distribution collapses towards the mid-plane as a result of radiative cooling removing thermal pressure support. The resulting high densities at the mid-plane allow stars to form, whose feedback begins to launch a nuclear outflow (see Section 2.1.1 for further details on our star formation and feedback methods). After 40 Myr the star formation and feedback cycle is well underway yet still quite similar for all physics cases. At this time we turn on the ICM wind (for non-`Isolated` runs). At 50 Myr (see Fig. 1) the ICM wind has just begun to interact with the `FaceOn` and `EdgeOn` runs. At this time, the `NoCR` runs have the most extended outflow structure, while the `ADV` runs have a relatively weak wind.

[5]That is, `ADV` can represent the limiting case of very slow CR transport, `NoCR` models the limit of very fast transport, and the diffusion coefficient adopted for `DIF` is a moderate value that should be near the peak wind driving efficiency (Salem & Bryan 2014) and is motivated by models of cosmic ray propagation (see Grenier, Black & Strong 2015 and references therein).

[6]This potential is consistent with observed rotation curves (Trachternach et al. 2008).

Downloaded from https://academic.oup.com/mnras/article/512/4/5927/6553836 by Columbia University user on 10 August 2022

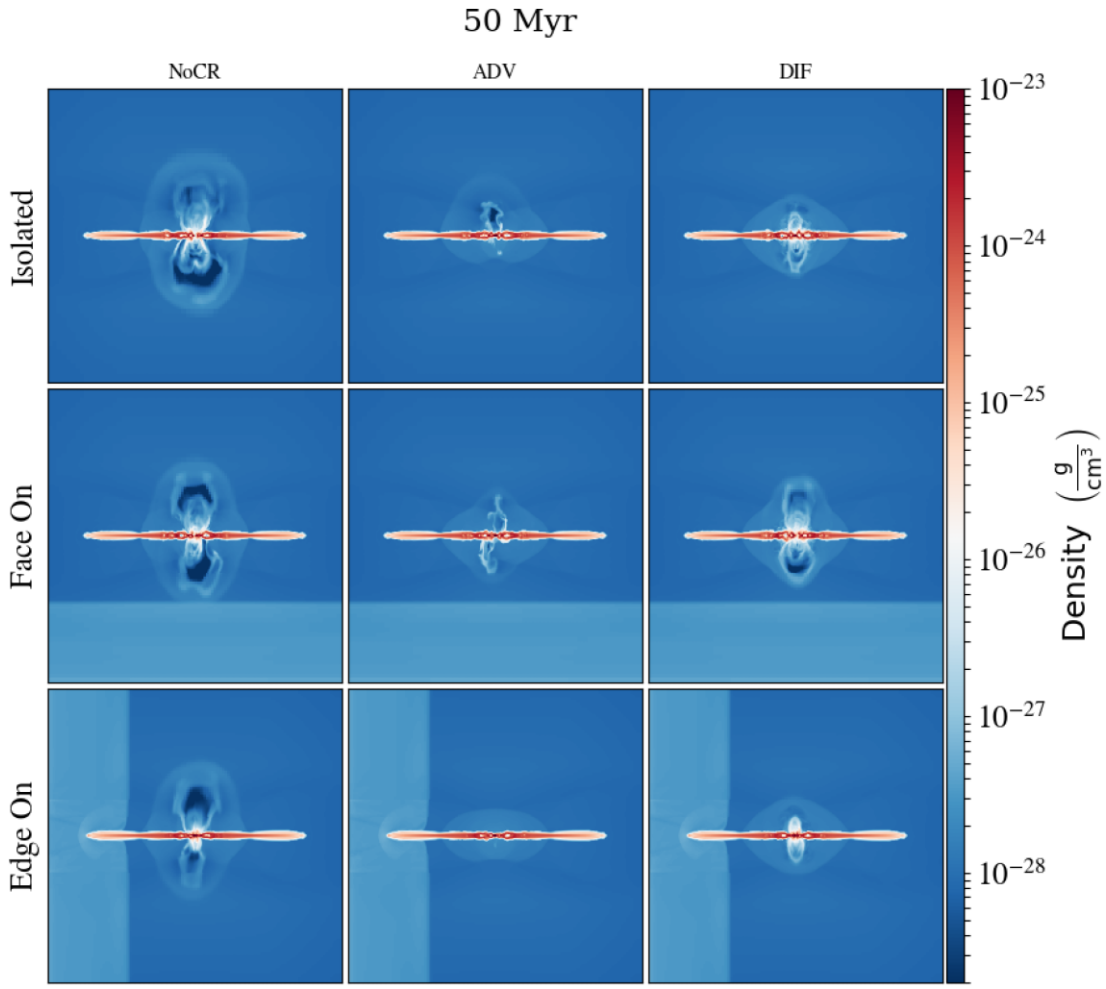

Figure 1. Slice plots at 50 Myr, shortly after the galaxies encounter an ICM wind (when appropriate). `NoCR` (left), `ADV` (middle), and `DIF` (right) physics cases are displayed for the `Isolated` (top), `FaceOn` (middle), and `EdgeOn` (bottom) runs. Red colours indicate high density, while blue colours indicate low densities.

As expected from the classical Gunn & Gott model for RPS, the ensuing ISM–ICM interaction proceeds from the outermost radii of the disc, where gas is beginning to be stripped by 100 Myr (see Fig. 2). The `Isolated` runs have now developed more extended galactic wind structures into the CGM. Note the `DIF` run has developed a frothy higher density galactic wind structure compared to the relatively low-density 'mushroom' ejecta of the `NoCR` case, while the weaker galactic wind in the `ADV` case has not propagated as far into the CGM as `NoCR` or `DIF`. The higher density outflow driven with CR is consistent with previous models of isolated galaxies with CR feedback (see Girichidis et al. 2018).

Meanwhile, cases with an ICM wind are beginning to diverge from their `Isolated` galaxy counterparts. Most noticeable is the higher density of the ICM ($\rho \sim 10^{-27}$ g cm^{-3}) compared to the CGM ($200\rho_{\rm crit} \sim 10^{-28}$ g cm^{-3}). In the `FaceOn` runs the development of a bowshock ∼20 kpc upstream of the disc is quite evident. Moreover, RPS has begun to affect the discs: the outermost portion of the discs are slightly bowed downstream from the RP of the colliding ICM wind.

For the `EdgeOn` runs the discs are slightly pushed downstream at 100 Myr (see Fig. 2), with notably absent galactic wind bubbles – stripping of galactic wind material has been 'caught-in-the-act' for the `DIF` case. Otherwise the galaxies in the `EdgeOn` case do not appear very disturbed.

As the ICM–ISM interaction proceeds, the `FaceOn` and `EdgeOn` cases diverge more drastically from the `Isolated` galaxies. At 175 Myr (see Fig. 3) the galactic winds of the `Isolated` runs have further developed. The `NoCR` run has evacuated a large-scale, biconical, low-density ($\rho \sim 10^{-29}$ g cm^{-3}) cavity from its nuclear region into the CGM, in shape reminiscent to the Fermi bubbles (Su, Slatyer & Finkbeiner 2010). In contrast, the `DIF` run has developed a frothy, disc-wide outflow whose relatively high-density ($\rho \sim 10^{-26}$ g cm^{-3}) is in better agreement with observations of the CGM (Werk et al. 2013). Note that stellar feedback similarly occurs to a larger radius in the disc now in the `NoCR` case as can be noted by the slightly thicker disc compared to the disc outskirts. In the `ADV` case, the outflow has largely shut off and the gas at large scale heights from the disc is returning in a fountain flow. The main impact of CR feedback in this case is the thickening of the gaseous disc due to the non-thermal pressure provided by CR, which efficiently suppresses star formation.

Meanwhile, the pushing of the now maximum RP wind (see Section 2.1 for the acceleration profile) has bowed back the `FaceOn` discs. Stripping from the ends of the warped disc gas downstream (and out of the computational domain) is evident possibly forming a tail structure (but studying the RPS tail is beyond the scope of this work). The high-density disc gas for the `FaceOn-ADV` run is thicker than the other physics cases. Reminiscent of the frothy outflow of the

Downloaded from https://academic.oup.com/mnras/article/512/4/5927/6553836 by Columbia University user on 10 August 2022

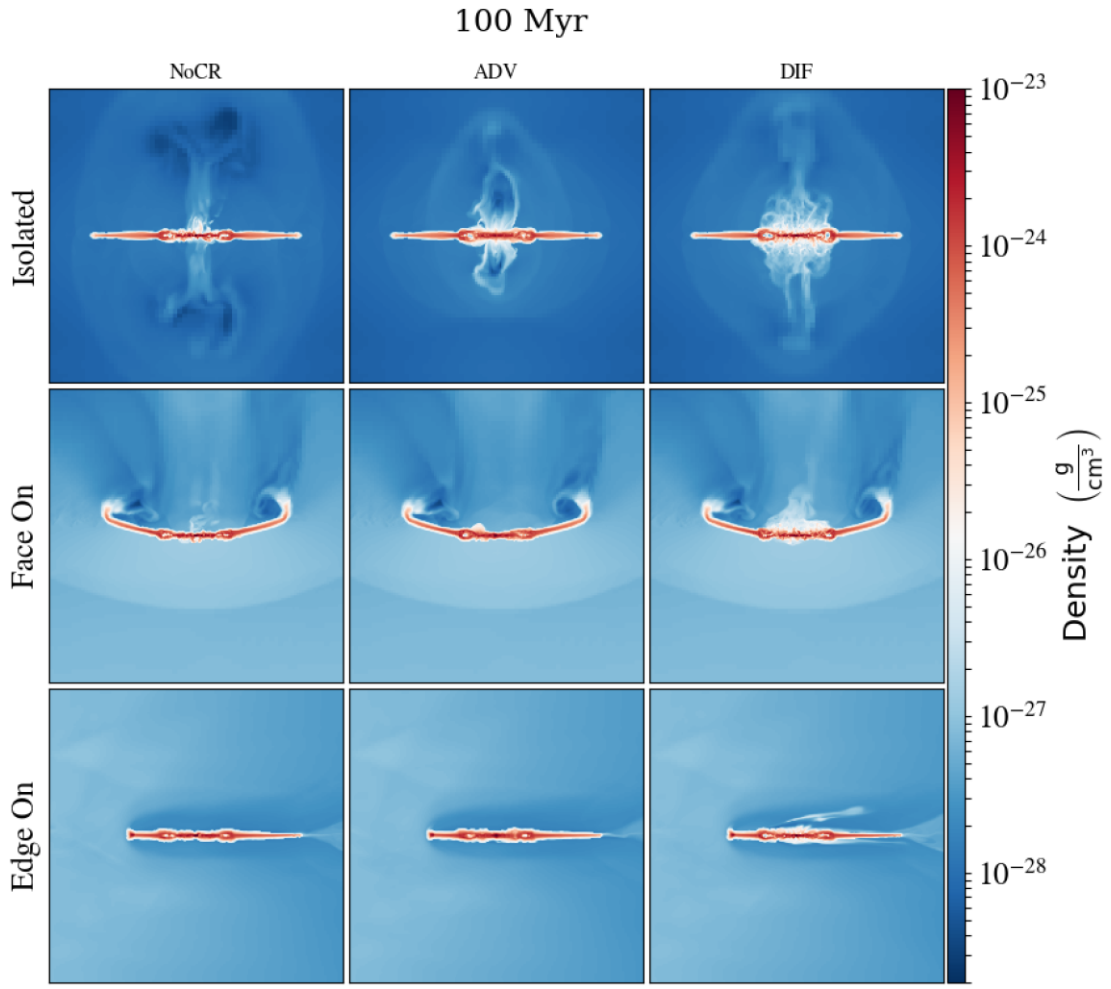

Figure 2. Same as Fig. 1 but at 100 Myr. Galactic winds have developed for the `Isolated` galaxies while for `FaceOn` disc gas is bowed backward due to RP. The galactic wind material is absent in the case of `EdgeOn` as it is readily stripped.

`Isolated` disc, the `FaceOn-DIF` case exhibits a low-density skin of gas surrounding the higher density mid-plane gas as seen in white in our slices. The low-density skin possesses a larger scale height downstream, as it is protected by the 'shadow' of the disc.

While the `FaceOn` discs are severely warped downstream, the `EdgeOn` discs appear to exhibit a fairly strong compression on the leading edge, forming a comet-like structure with a distinct high-density 'head' just upstream of (stellar) galactic centre and a tail of dense disc gas downstream. Again, the `ADV` run exhibits a somewhat thicker structure of dense disc gas, while the `DIF` galaxy possesses a low-density skin, as an outflow (which is rapidly stripped) is driven by diffusing CR.

While we have indicated the most salient differences between our CR physics cases, the most striking observation is how relatively *similar* the morphology is for galaxies subjected to RPS. This is shocking especially after one considers the radical differences of the galactic winds of the `Isolated` cases. Nevertheless, previous studies have found RPS proceeds at a rate largely unaffected by non-thermal forces (e.g. magnetic fields, see Ruszkowski et al. 2014; Tonnesen & Stone 2014), as suggested by the good agreement between observations and the Gunn & Gott criterion. In the next section, we investigate the impact of CR on the RPS rate.

3.2 Stripping

To determine the impact of CR physics on the RPS rate, we investigate the amount of gas remaining in the disc in our simulations. We define disc gas as possessing a tracer fraction $C > 0.6$ contained within a cylinder of radius 28.6 kpc and height ± 1 kpc from the disc mid-plane.

In Fig. 4, we show the mass in the disc as a function of time for our nine simulations. The solid, dashed, and dotted lines indicate the `FaceOn`, `EdgeOn`, and `Isolated` runs, respectively, while the blue circles, the red triangles, and the green stars represent `NoCR`, `ADV`, and `DIF` physics cases, respectively. During the first 40 Myr the disc mass increases due to radiative-cooling-induced collapse on to the disc mid-plane. The disc mass stabilizes until ∼75 Myr when the impact of the ICM wind begins to differentiate the evolution.

From 75–150 Myr the `FaceOn` runs are efficiently stripped of ∼80 per cent of their disc mass. As some stripped material enters the 'shadow' of the remaining disc and is protected from acceleration to the escape velocity, some material falls back on to the disc from ∼175 to 230 Myr. In contrast, the `EdgeOn` runs are more slowly stripped (maintaining $\gtrsim$90 per cent of their initial disc gas mass by 150 Myr and ∼60 per cent by 230 Myr) owing to the reduced cross-section for ISM–ICM interaction, in agreement with previous work

Downloaded from https://academic.oup.com/mnras/article/512/4/5927/6553836 by Columbia University user on 10 August 2022

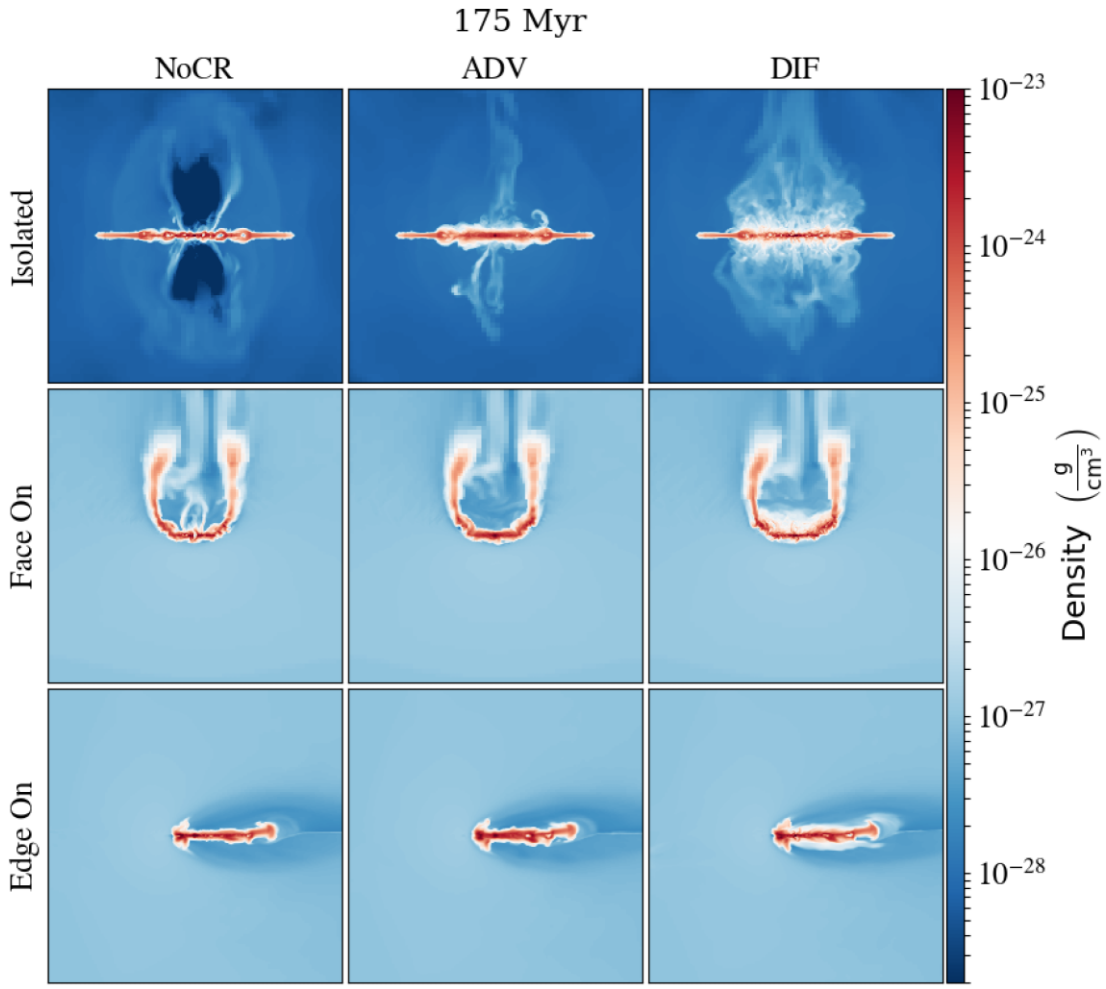

Figure 3. Same as Fig. 1 but at 175 Myr. The `Isolated` galaxies' winds have continued to expand into the CGM. The `FaceOn` and `EdgeOn` galaxies' discs are distorted due to the RP of the ICM wind.

Table 2. Nomenclature.

Name	Description
$f_{\rm th}$	Thermal fraction of SN energy.
$f_{\rm cr}$	Cosmic ray fraction of SN energy.
dx	Cell width.
MHD	Magnetohydrodynamics.
USM	Unsplit Staggered Mesh.
RPS	Ram Pressure Stripping.
SFR	Star Formation Rate.
SNe	Supernovae.
ICM	Intra-cluster Medium.
CGM	Circum-galactic Medium.
`Isolated`	No ICM wind.
`FaceOn`	ICM wind parallel to galactic spin axis.
`EdgeOn`	ICM wind perpendicular to galactic spin axis.
`NoCR`	No cosmic rays.
`ADV`	Cosmic rays only advect.
`DIF`	Cosmic rays advect and diffuse.

(Roediger & Brüggen 2006; Jáchym et al. 2009). The `EdgeOn` runs lack a fallback episode owing to the lack of protective 'shadow.'

Meanwhile, the `Isolated` runs maintain most of their disc mass as expected with the disc gas mass-loss due primarily to galactic winds. Interestingly, the `ADV` run ejects more disc gas mass initially than the `NoCR` run due to the contrast between the hot, low-density cavities driven in the `NoCR` case compared to the `ADV` case (see Fig. 3). Both `ADV` and `DIF` runs exhibit periodic fountain flows (see the oscillatory behaviour of the dotted lines) or accretion dominating over the outflow, whereas the `NoCR` disc gas mass is monotonically decreasing.

As anticipated from the largely similar evolution of the `NoCR`, `ADV`, and `DIF` cases of the `FaceOn` and `EdgeOn` runs (see Figs 1–3), the stripping rates do not differ widely between the physics cases (not more than ∼15 per cent, see Fig. 4). However, knowing that the `Isolated` runs produce quite distinct galactic wind structures, the fact that CRs play a minor role in the removal of gas from RPS galaxies is quite surprising. Nevertheless, we find CR physics does play a role in modifying the temperature-density phase space of cluster spirals, which we discuss next.

Downloaded from https://academic.oup.com/mnras/article/512/4/5927/6553836 by Columbia University user on 10 August 2022

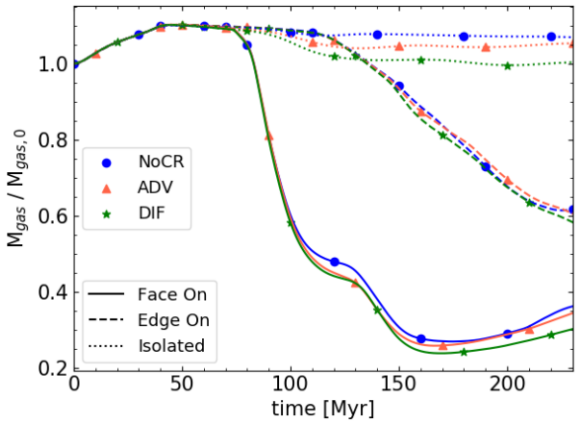

Figure 4. Evolution of the gas mass in the disc as a function of time. We define disc gas mass to possess a concentration tracer threshold $C > 0.6$ within a cylinder of radius 28.6 kpc and height ± 1 kpc from the mid-plane.[7] CR physics cases NoCR, ADV, and DIF are indicated as blue circles, red triangles, and green stars, while the ICM wind types are indicated as solid, dashed, and dotted curves for FaceOn, EdgeOn, and Isolated respectively. The stripping rate appears to be fairly insensitive to CR physics.

3.3 Gas phase distribution in the disc

While the morphology and stripping rates are similar across our three CR physics cases (NoCR, ADV, and DIF), examining the galactic disc in detail suggests CRs play an interesting role in modifying galactic properties. We start with the phase space distributions of disc[8] gas temperature and density at 175 Myr in Fig. 5. The columns from left to right show NoCR, ADV, and DIF physics cases, and the rows from top to bottom display Isolated, FaceOn, and EdgeOn runs.

In agreement with previous work, the Isolated runs (top row) indicate that including CRs permits the presence of low-density, low-temperature gas, as they provide non-thermal pressure support (Butsky et al. 2020; Ji et al. 2020). Note the low-temperature ridge at $T \sim 10^2$ K is weak in NoCR runs (supported only by magnetic pressure in those cases). The low-temperature ridge is dimmer (less yellow) for the DIF run related to less CR pressure in the disc supporting that gas. The ridge has a low-mass component extending to lower temperatures in the DIF case related to adiabatic cooling of the galactic wind.

Note that once the wind has impacted the galaxies, we expect that low-density gas will be preferentially removed due to its lower restoring force. Indeed, in the NoCR run this is clearly seen in both the FaceOn and EdgeOn runs at all temperatures. We also see a small increase in the amount of dense gas, particularly in the EdgeOn run, in agreement with our visual impression of gas compression in Figs 1–3.

However, the gas distribution is somewhat different in the stripped galaxies with CR. While above $\sim 10^4$ K, low-density gas seems to be removed, at cooler temperatures more low-density gas survives than in the NoCR wind runs (highlighted by the red boxes). We can understand this by the low-temperature ridge in the isolated versus wind runs.

[7]Note the results depend very weakly on the value of C (we considered values ranging from 0.1–0.9 to confirm but used 0.6 as in previous work).

[8]Note that we select 'disc' gas by applying a concentration threshold of $C > 0.6$ and require gas to fit within a cylinder of radius 28.6 kpc and height ± 1 kpc from the mid-plane.

The low-temperature ridge is at slightly lower temperatures when RPS is turned on due to enhanced non-thermal pressures. An elevated magnetic field strength due to compression of the disc is the source of non-thermal pressure in the NoCR case. The low-temperature ridge gets brighter when including CR and is brighter for ADV than DIF related to the concentration of CR in the disc. As we will show, CR production is enhanced due to increased SFRs with RP. The low-temperature feature extends to lower temperature in the DIF case due to CR outside the disc. Although CR are swept away quickly in the EdgeOn case (as seen in Fig. 3), they are also constantly replenished by star formation and subsequent feedback. In summary, the inclusion of CRs allows low-temperature, low-density gas to survive in RP discs due to an increase in non-thermal pressure.

The NoCR runs show that RPS efficiently strips low-density gas. However, galaxies subjected to RPS (middle and bottom rows) including CR (middle and right columns) contain low-density gas that is otherwise stripped in the NoCR runs (left column; bottom left portion of each plot). Further evidence that RP removes low-density gas, yet CRs support the existence of such gas is provided by Fig. 6.

Probably the most interesting result is that RPS increases the amount of low-temperature gas and this RPS-induced effect is stronger when CR are included (see Section 5).

3.4 Star formation

Let us begin by examining the physical SFR in the top panel of Fig. 7. As previously, we use blue circles, red triangles, and green stars to, respectively, indicate NoCR, ADV, and DIF cases, while the solid, dashed, and dotted lines refer to the ICM wind cases of FaceOn, EdgeOn, and Isolated, respectively. All physics cases and ICM wind runs have similar SFR up to roughly 100 Myr. After that point, the ICM–ISM interaction begins to take effect with the SFRs clearly diverging. For all ICM wind runs, NoCR, DIF, and ADV clearly have the highest to lowest respective SFRs with the EdgeOn runs exhibiting demonstrably higher SFR than FaceOn runs at 175 Myr (see Appendix A for a discussion of convergence).

Comparing the SFR of RPS galaxies to their isolated counterparts is more readily achieved looking at ratios in the bottom panel of Fig. 7. Again, we observe significant departures in the SFRs of different ICM wind or CR physics cases only after 100 Myr. Subsequently, FaceOn-DIF and FaceOn-NoCR show moderate enhancement of SFR over their Isolated counterparts in best agreement with observations (∼0.2–0.4 dex enhancement of star formation, Vulcani et al. 2018; Roberts et al. 2021).

The FaceOn-ADV run achieves peaks of four to six times the value of Isolated-ADV (which is largely quiescent due to the build-up of CR energy). The NoCR-EdgeOn run similarly initially attains a boost four times the Isolated run at 175 Myr. The EdgeOn-ADV run shows the most dramatic boost in SFR, exceeding an order of magnitude at ∼175 Myr. Since a fluid dominated by CR has an adiabatic index of 4/3, whereas a thermal plasma has an adiabatic index of 5/3, the CR fluid is more compressible. Thus, when the ICM wind impacts the disc in the ADV run which is dominated by cosmic pressure, there is a larger increase in the density than the DIF or NoCR cases, explaining the boost in SFR.

Clearly, the EdgeOn-ADV run is inconsistent with the much more modest boosts in star formation observed (∼0.2 dex by Vulcani et al. 2018 and ∼0.4 dex by Roberts et al. 2021); in fact, all the EdgeOn runs appear to be inconsistent with observations. Roediger & Brüggen (2006) found inclination makes a minor difference to RPS until $\gtrsim 60°$, suggesting most spiral galaxies falling into a cluster can be modeled as FaceOn. Although both FaceOn-DIF and

Downloaded from https://academic.oup.com/mnras/article/512/4/5927/6553836 by Columbia University user on 10 August 2022

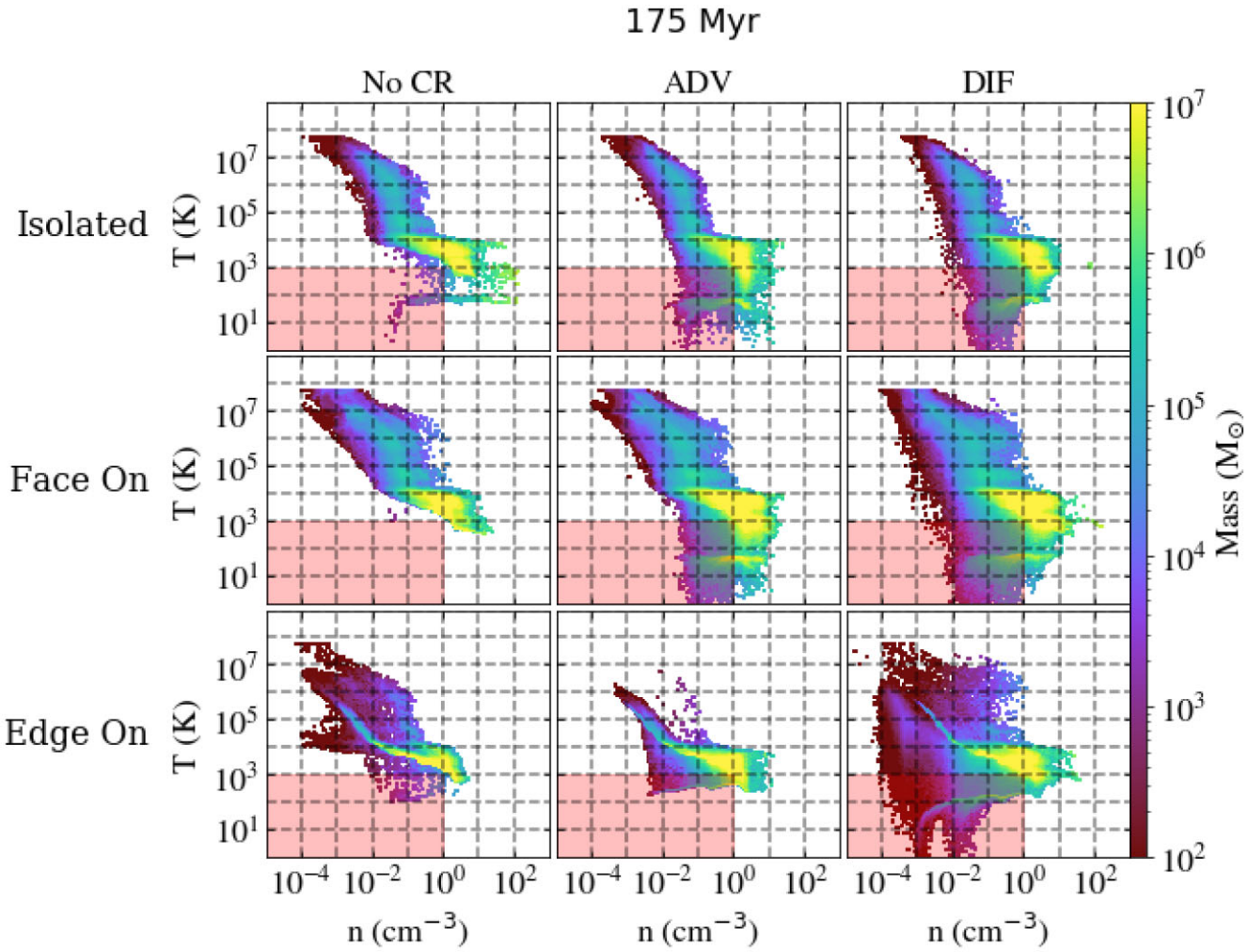

Figure 5. Gas temperature versus number density phase plots at 175 Myr. The left, centre, and right columns display NoCR, ADV, and DIF physics cases respectively, while the top, middle, and bottom rows show Isolated, FaceOn, and EdgeOn ICM wind (or lack thereof) run types. Bright (dark) colours indicate regions with much (little) gas mass. The dashed lines are intended to ease comparison across the various runs. The red highlighted regions of low temperature and low density highlight the influence of CRs in allowing such a phase to persist.

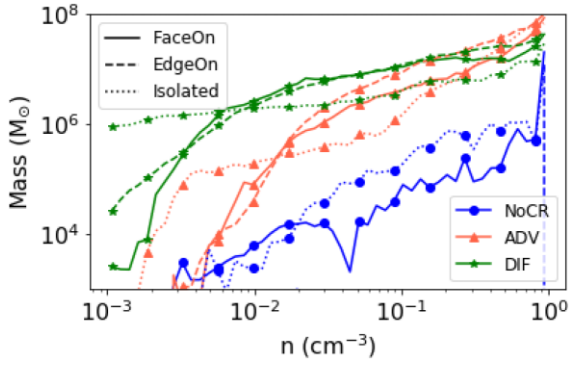

Figure 6. Mass-weighted histogram of gas number density at 175 Myr. The NoCR, ADV, and DIF physics cases are shown as blue, red, and green curves, respectively, while the FaceOn, EdgeOn, and Isolated ICM wind (or lack thereof) run types are indicated by solid, dashed, and dotted linestyles respectively. The Isolated runs typically have larger masses of low-density gas, and the cases with CR clearly exhibit larger masses of low-density gas than NoCR.

FaceOn-NoCR are consistent with observed SFR enhancements, the degeneracy may be broken when we consider the evolution of mass at the galactic centre below.

3.5 Feeding the AGNs: accretion on to the galactic centre

While the SFR plots appear degenerate between the DIF and NoCR models, the galactic accretion rate (Fig. 8) appears to tell a different story. The top panel indicates the accretion rate of material flowing in the disc plane towards the galactic centre. That is, we select disc gas (tracer concentration $C > 0.6$ within a cylinder of radius 28.6 kpc and height ± 1 kpc from the mid-plane) and take a one-dimensional profile of the radially inward flowing velocity. We time-average the radial velocity at each radius from 100 to 230 Myr.[9] We indicate the NoCR, ADV, and DIF models as blue circles, red triangles, and green stars, respectively, with the FaceOn, EdgeOn, and Isolated galaxies marked as solid, dashed, and dotted lines, respectively. In general, we see that RPS galaxies have enhanced accretion rates, in

[9]The SFR begins to diverge between the different runs at 100 Myr. We confirmed our results averaging 50–230 Myr.

Downloaded from https://academic.oup.com/mnras/article/512/4/5927/6553836 by Columbia University user on 10 August 2022

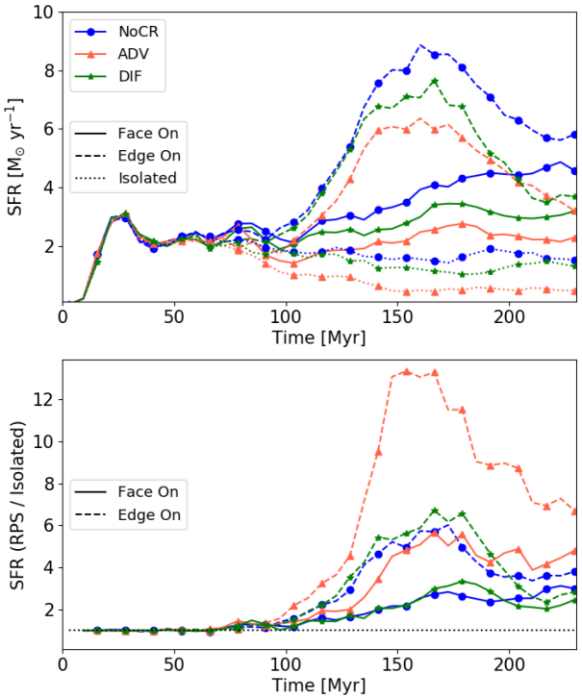

Figure 7. Time series of SFR (top) and ratio of SFR of the FaceOn (solid) or EdgeOn (dashed) runs to the Isolated (dotted) runs. NoCR, ADV, and DIF are marked as blue circles, red triangles, and green stars, respectively. Clearly, the NoCR runs have the highest SFR and ADV receives on average the largest boost in SFR when a galaxy is subjected to an ICM wind.

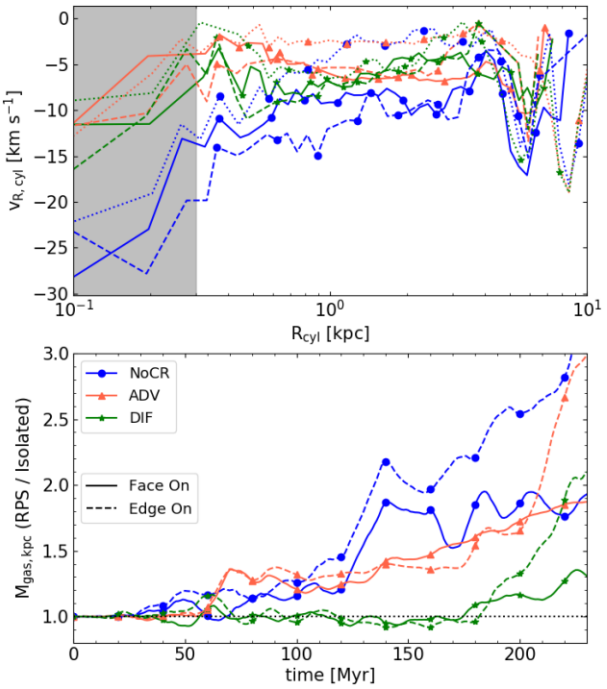

Figure 8. Top: Time-averaged negative (gas flowing towards the galactic centre) cylindrical radial velocity as a function of cylindrical radius. The grey region samples less than 10 cells linearly so we caution against overinterpretation. Bottom: galactic centre mass ratios of RPS runs to Isolated counterparts, in this case defined as a sphere of radius 1 kpc centred on the galactic centre. NoCR, ADV, and DIF physics cases are shown as blue circles, red triangles, and green stars, respectively. FaceOn and EdgeOn ratios are indicated by the solid and dashed markers, respectively.

qualitative agreement with observations finding RPS galaxies have higher AGN fractions than galaxies in the field (Poggianti et al. 2017a; Radovich et al. 2019; Peluso et al. 2022). Moreover, the runs with CR appear to suppress galactic accretion, as the NoCR run clearly has the strongest accretion rate independent of inclination. Together with the SFR results, this suggests CR must be more weakly coupled to the disc gas. That is, either CR are transported faster or they rapidly experience strong Coulomb and hadronic losses. The accretion rate for the Isolated runs appears to be consistent with recent cosmological models that also find CRs suppress accretion (Trapp et al. 2022).

For a clearer picture of the accretion on to the galactic centre, we show in the bottom panel of Fig. 8 the time evolution of the gas[10] mass within a sphere of radius 1 kpc emanating from the galactic centre as a ratio of RPS runs to their Isolated counterparts. For example, we indicate with a blue solid curve the central 1 kpc gas mass for the ratio of FaceOn-NoCR to Isolated-NoCR. Until about 100 Myr, the galactic central mass is largely indistinguishable between ICM wind types and CR physics cases (∼20 per cent difference). Subsequently, the ISM–ICM interaction drives accretion towards the galactic central region. The non-thermal pressure of CR suppresses accretion and as a result, the central gas mass is nearly double for FaceOn-NoCR compared to that for FaceOn-DIF. In general, the NoCR runs exhibit the largest central masses followed by the ADV and then DIF runs.

At the end of our simulations, the DIF run has the least mass accreted in the galactic centre. This may suggest CRs suffer strong calorimetric losses, or that the diffusion coefficient must be much faster to reduce the coupling to disc gas, if strong accretion is required to match observations of high AGN fraction in RPS galaxies. However, we note that although weaker, the DIF RPS runs nevertheless have an elevated accreted mass in the galactic centre compared to Isolated (that is, the ratio is greater than one); it would be interesting if future work can tease out the required accretion to trigger AGNs.

Note that even in the Isolated runs the galactic centre mass increases by a factor of two for CR runs and a factor of four for NoCR (not shown here). Our magnetized disc is subject to the magnetorotational instability (MRI; Balbus & Hawley 1991) beyond ∼4 kpc where the angular velocity begins to diminish radially outwards (Hawley & Balbus 1999). Since the MRI growth rate is proportional to orbital frequency, growth is strongest for the inner parts of the disc (e.g. ∼120 Myr at 4 kpc and ∼800 Myr at the disc edge; for more discussion see Tonnesen & Stone 2014). We also expect gravitational torques (i.e. self-gravity) to transport angular momentum. Thus, we expect some accretion of mass towards the galactic centre even for Isolated. Moreover, since the magnetic field in the disc is strengthened for discs subjected to RPS (see middle panel of Fig. 9), the increase in accretion for RPS runs compared to Isolated could be due to more efficient MRI.

The enhanced accretion of NoCR runs over those with CR, particularly over DIF runs, is potentially constraining of CR transport and calorimetry.

3.6 Radio emission

RPS galaxies are observed to possess enhanced global radio emission (as recently confirmed in Persues; Roberts et al. 2022), existing as outliers to the otherwise very tight FRC (Murphy et al. 2009; Vollmer

[10]Note that the mass converted into stars is relatively modest and does not impact our conclusions.

Downloaded from https://academic.oup.com/mnras/article/512/4/5927/6553836 by Columbia University user on 10 August 2022

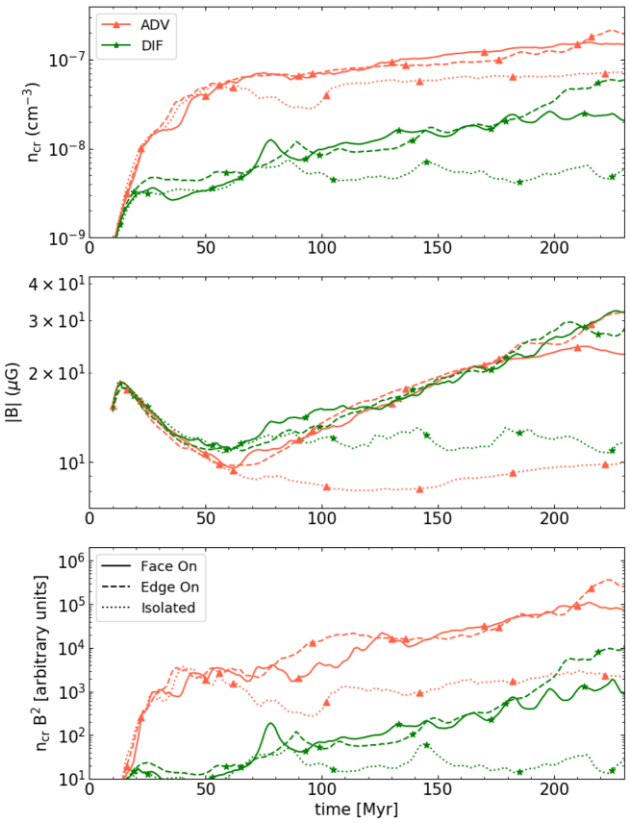

Figure 9. Time series profiles of CR number density (top), magnetic field strength (middle), and proxy for radio synchrotron (bottom). The red triangles (green stars) curves indicate ADV (DIF) physics cases. The solid, dashed, and dotted curves indicate FaceOn, EdgeOn, and Isolated runs, respectively. RPS both boosts |B| and n_{cr} by a factor of a few, producing a ∼2 mag boost in expected radio emission.

et al. 2013). However, it is unclear if the excess compared to the FRC is due to stronger magnetic fields, elevated CR number densities n_{cr}, or both. In Fig. 9, we determine the relative contribution of these components to a synchrotron radio emission proxy ($n_{cr}B^2$).

In the top panel of Fig. 9 we see that RPS elevates the n_{cr} by a factor of a few for ADV runs and about 1 mag for DIF runs compared to their Isolated galaxy counterparts, likely related to RPS boosting the SFR (see Fig. 7). We highlight that the lower n_{cr} for DIF compared to ADV must be due to the transport of CR out of the galactic disc, as more CRs are injected for the DIF run (it has a higher SFR than ADV). Similarly, the boost in n_{cr} is very similar in the FaceOn and EdgeOn runs even though the boost in SFR is different, again suggesting transport dominates the n_{cr} evolution. Surprisingly, ADV has a smaller boost in n_{cr} despite having a larger boost in SFR than DIF for runs including RPS. This may suggest fewer CR are stripped in the DIF case. Clearly, exploring the boost in n_{cr} represents an interesting avenue for future research.

Yet the elevated radio emission in RPS galaxies is not only due to the elevated CR number density; in the middle panel of Fig. 9 we see that the magnetic field strength is similarly boosted by a factor of a few. We also note that the magnetic field strength in the NoCRruns is boosted by a similar amount. It is somewhat surprising that the magnetic field strength is so similar for all runs with a wind, independent of CR transport or wind orientation. On the one hand, one would expect stronger magnetic field strengths for the EdgeOn runs as they exhibit higher SFRs (see top panel of Fig. 7). On the other hand, compression of the disc magnetic field should be more effective for the FaceOn run, given the larger cross-sectional area of the galaxy presented to the ICM wind. We plan on disentangling these effects in future work.

However, since the synchrotron emission depends steeply on the magnetic field strength, the combined effect is a boost of 2–3 mag, as seen in the bottom panel of Fig. 9.

Clearly, CR transport plays a crucial role in driving the radio emission. We neglect more detailed analysis such as considering spatial maps of the radio emission with comparison to observations of local deficits observed by Murphy et al. (2009) as our CR model follows the protons, whereas electrons generate the radio emission via synchrotron emission. Future work will use a spectral treatment of CR (Yang & Ruszkowski 2017) to directly model the propagation and cooling of CR primary electrons, as well as the generation of secondaries.

3.7 Implications for Jellyfish galaxies

Recent observations have discovered multiphase tails of stripped gas, extending up to ∼100 kpc from the disc (see Poggianti et al. 2017b). Detections of molecular gas and star formation (e.g. Moretti et al. 2018) in these tails are difficult to reconcile with theoretical work suggesting dense gas is not readily stripped (e.g. Tonnesen & Bryan 2012). Regardless of the removal, cold, molecular gas should be rapidly heated and mixed with the ambient hot ICM (Cowie & McKee 1977; McKee & Cowie 1977; Balbus & McKee 1982; Stone & Norman 1992; Klein, McKee & Colella 1994; Mac Low et al. 1994; Xu & Stone 1995). In contrast, the presence of star formation suggests stripped gas not only survives but attains sufficient mass to induce gravitational collapse.

High-resolution 3D cloud-crushing simulations suggest efficient radiative cooling enable clouds to not only survive but grow in mass (Gronke & Oh 2018, 2020; Sparre, Pfrommer & Ehlert 2020; Li et al. 2020; Kanjilal, Dutta & Sharma 2021; Abruzzo, Bryan & Fielding 2022; Farber & Gronke 2022). Tonnesen & Bryan (2021) study the survival of cold clouds in RPS tails, finding the fate of cold gas may depend on ICM properties. Even in the destruction regime, molecular material may form on short time scales when dust is present (Girichidis et al. 2021).

We find that CRs provide non-thermal pressure support for a diffuse molecular phase (see Fig. 5). At later times when a galaxy encounters the higher density of cluster cores, it is likely this diffuse molecular gas will be stripped, even if dense molecular cores remain unperturbed. If blobs of diffuse molecular gas are sufficiently large to satisfy the Farber & Gronke criteria then these clouds may grow in mass and eventually become star-forming. However, the impact of CR on cloud crushing remains relatively unexplored (see Wiener, Pfrommer & Oh 2017; Wiener et al. 2019; Brüggen & Scannapieco 2020; Bustard & Zweibel 2021). In future work, we will explore these issues in greater depth.

4 CAVEATS AND FUTURE WORK

4.1 Resolution

Our physical resolution of ∼127 pc is similar to that used in previous works including magnetic fields (Ruszkowski et al. 2014; Tonnesen & Stone 2014; Ramos-Martínez et al. 2018). Although we include non-thermal physics and stellar feedback neglected by previous hydrodynamical studies, it is true such hydro studies were performed at high resolution (∼40 pc) limiting the ability to compare with our work. We plan on running higher resolution models in future work.

Downloaded from https://academic.oup.com/mnras/article/512/4/5927/6553836 by Columbia University user on 10 August 2022

4.2 Box size

Our relatively small box size ($\sim$64 kpc)^3 and resolution degrading from the galactic disc limits our ability to study the fate of stripped gas: do CRs enable stripping of diffuse molecular material that can survive and compose observed molecular tails? Do CRs couple with the stripped gas? How do observed radio tails constrain CR transport? We plan to investigate such stimulating problems in future work.

4.3 Wind profile

We utilized a relatively simple model for the relative motion between our simulated galaxy and ICM. That is, we assume a fixed magnetic field strength, density, and temperature. We do vary the wind velocity, modelling the galaxy falling from rest into the cluster; however, we have a constant wind for $\sim$150 Myr (for the ICM wind details, see Section 2.1). In reality, a galaxy falling into a cluster should sample a hotter, denser, and faster wind as it plunges towards the centre of the cluster and diminishing thereafter. We note that the time we simulate the galaxy only traverses $\lesssim$0.3 Mpc. Thus, our galaxy samples cluster outskirts and our model is not implausible.

4.4 Momentum feedback

We utilized a momentum boost factor of five to account for unresolved clustering of supernovae as well as to account for advection errors. While observations clearly find the average kinetic energy ejected by supernovae to be 10^{51} erg, the coupling with the ambient ISM is highly uncertain. Several idealized, high-resolution studies have investigated the impact that clustered supernovae have on the momentum injected (coupled) to the ISM per supernova with varying results. Kim & Ostriker (2015) find previous generations of bubbles decrease the injected momentum by a factor of two (similar to Pittard 2019). Meanwhile, Walch & Naab (2015) find the momentum injected should be at least 25 per cent higher than the case of isolated supernovae, with Gentry et al. (2017) finding up to an order-of-magnitude larger and Keller et al. (2014) about five times larger. Additionally, Diesing & Caprioli (2018) find that CRs may boost the momentum injected by up to an order of magnitude. Recently, Montero et al. (2022) performed 3D cosmic ray MHD simulations of isolated supernovae in homogeneous medium and found that including CRs increases the momentum deposition by at least 50 per cent with a higher impact at lower ambient densities (as would be the case for clustered supernovae). Thus, our choice of a boost factor of five is within the plausible range, which will hopefully be more tightly constrained by future work. Moreover, since our results are based on comparisons between different runs with all runs using the same boost factor, we do not expect our results to be impacted.

4.5 Neglected Physics

CRs are efficiently coupled to thermal plasma by scattering off waves they self-excite. The distribution of CRs thus drifts with respect to the thermal plasma at the local Alfvén velocity (Kulsrud & Pearce 1969; Zweibel 2017). However, wave damping processes such as ion-neutral friction (Kulsrud & Cesarsky 1971; Farber et al. 2018; Bustard & Zweibel 2021), turbulent damping (Farmer & Goldreich 2004; Lazarian 2016; Holguin et al. 2019), linear Landau damping (Wiener, Zweibel & Oh 2018), and non-linear Landau damping (Kulsrud 2005) enable CR to stream super-Alfvénically and enable CRs to heat the gas (mediated by the growth and subsequent damping of hydromagnetic waves).

Our neglect of CR streaming in addition to collisional loss processes (e.g. Coulomb and hadronic) will reduce the CR energy, transferring it to the thermal gas. However, our `NoCR` runs can effectively model CR losses proceeding very rapidly and thus comparison between the `NoCR`, `ADV`, and `DIF` simulations should bracket the inclusion of CR losses. The enhanced transport of CR away from the cold, dense mid-plane due to ion-neutral damping may help to reduce CR suppression of the centralized accretion flow we observe in our simulations, see Fig. 8.

However, significant uncertainties in CR transport remain (Hopkins et al. 2021). Recent work suggests CR may not completely decouple in the neutral medium (due to the 'bottleneck' effect; Wiener et al. 2017, 2019; Bustard & Zweibel 2021) if pressure anisotropy can act as an efficient mechanism to grow hydromagnetic waves (Zweibel 2020). Even in the absence of pressure anisotropy, dust grains may grow (or damp, depending on their transport relative to the Alven speed) hydromagnetic waves, even in molecular phases of low ionization fraction (Squire et al. 2021). Exploring detailed models of (novel) CR transport is beyond the scope of this work. Importantly, our results suggest CR transport can be effectively constrained in RPS studies, motivating future work on this topic.

We additionally ignore physics such as radiation pressure, anisotropic conduction, viscosity, and interactions with external galaxies as they are beyond the scope of this paper.

5 CONCLUSIONS

We performed the first CR MHD simulations of an L_* cluster galaxy subjected to RPS, including radiative cooling, self-gravity of the gas, star formation, and stellar feedback. Our main conclusions are summarized as follows.

(i) CRs do not dramatically change the RPS rate. This is true for the extreme cases of pure CR advection and diffusion without collisional losses and independent of the galaxy's inclination to the ICM wind. In all cases the stripping rates do not differ by more than $\sim$15 per cent in the 230 Myr of evolution we simulate.

(ii) The non-thermal pressure provided by CRs permits a stable low-temperature, low-density phase, which persists even with RPS. Since low-density gas is typically preferentially stripped, the additional CR pressure likely supports this gas against RPS. Interestingly, RPS increases the amount of low-temperature gas in discs surviving both face-on and edge-on winds, particularly when CRs are included.

(iii) The observed *moderate* enhancement of star formation for cluster spirals undergoing RPS places strong constraints on our models. Most of our simulations exhibit too large of a boost, attaining values approximately four to six times greater for ram-pressure-stripped galaxies compared to isolated ones. We highlight that all of the `ADV` simulations overenhance SFRs with respect to observations, while the `FaceOn-NoCR` and `FaceOn-DIF` models are in plausible agreement with the observed enhancement.

(iv) We find that CRs suppress accretion of gas along the disc towards the mid-plane, even in isolated cases. Conversely, observations of cluster spirals indicating a high AGN fraction and bulge-dominated spirals (density–morphology relation) suggest enhanced gas accumulation in the nuclear region of galaxies undergoing RPS. These observations appear to favour CRs suffering rapid catastrophic losses or very efficient transport out of the disc. We suggest observations of ram-pressure-stripped galaxies may place novel constraints on CR physics.

Downloaded from https://academic.oup.com/mnras/article/512/4/5927/6553836 by Columbia University user on 10 August 2022

(v) In agreement with radio observations, our galaxy models suggest that ram-pressure-stripped galaxies boast of enhanced radio emission compared to their counterparts in the field. We find magnetic field strengths boosted by a factor of a few, and CR number densities enhanced by a factor of 10 for the diffusion model and by a factor of a few for the advection model. CR transport thus may play a crucial role in understanding the enhanced radio emission above the FIR to FRC for cluster spirals.

ACKNOWLEDGEMENTS

RJF gratefully acknowledges Dongwook Lee for helpful discussions. RJF thanks the Kavli Institute for Theoretical Physics for hospitality during part of this project as part of the Graduate Fellowship Program. This research was supported in part by the National Science Foundation under Grant No. NSF PHY-1748958. MR acknowledges support from NSF Collaborative Research Grants AST-1715140 and AST-2009227 and NASA grants 80NSSC20K1541 and 80NSSC20K1583. ST acknowledges support from the Center for Computational Astrophysics at the Flatiron Institute, which is supported by the Simons Foundation. This project utilized the visualization and data analysis package `yt` (Turk et al. 2010); we are grateful to the yt community for their support.

DATA AVAILABILITY

The simulation and data analysis scripts utilized to obtain the results presented in this paper will be shared on reasonable request to the corresponding author.

REFERENCES

Abruzzo M. W., Bryan G. L., Fielding D. B., 2022, ApJ, 925, 199
Agertz O., Kravtsov A. V., Leitner S. N., Gnedin N. Y., 2013, ApJ, 770, 25
Balbus S. A., Hawley J. F., 1991, ApJ, 376, 214
Balbus S. A., McKee C. F., 1982, ApJ, 252, 529
Beck R., Golla G., 1988, A&A, 191, L9
Bekki K., 2013, MNRAS, 438, 444
Booth C., Agertz O., Kravtsov A. V., Gnedin N. Y., 2013, ApJ, 777, L16
Boselli A., Gavazzi G., 2006, PASP, 118, 517
Brüggen M., Scannapieco E., 2020, ApJ, 905, 19
Burkert A., 1995, ApJ, 447, L25
Bustard C., Zweibel E. G., 2021, ApJ, 913, 106
Bustard C., Zweibel E. G., D'Onghia E., Gallagher J. III, Farber R., 2020, ApJ, 893, 29
Butcher H., Oemler A. Jr, 1978, ApJ, 226, 559
Butsky I. S., Quinn T. R., 2018, ApJ, 868, 108
Butsky I. S., Fielding D. B., Hayward C. C., Hummels C. B., Quinn T. R., Werk J. K., 2020, ApJ, 903, 77
Chan T. K., Kereš D., Hopkins P. F., Quataert E., Su K.-Y., Hayward C. C., Faucher C.-A., Ere G., 2019, MNRAS, 488, 3716
Cowie L. L., McKee C. F., 1977, ApJ, 211, 135
Dickey J., Salpeter E., 1984, ApJ, 284, 461
Diesing R., Caprioli D., 2018, Phys. Rev. Lett., 121, 091101
Dressler A., 1980, ApJ, 236, 351
Dubey A., Reid L. B., Fisher R., 2008, Phys. Scr., 2008, 14046
Dursi L., Pfrommer C., 2008, ApJ, 677, 993
Enßlin T. A., Pfrommer C., Springel V., Jubelgas M., 2007, A&A, 473, 41
Everett J. E., Zweibel E. G., Benjamin R. A., McCammon D., Rocks L., Gallagher J. S. III, 2008, ApJ, 674, 258
Farber R., Ruszkowski M., Yang H.-Y., Zweibel E. G., 2018, ApJ, 856, 112
Farber R. J., Gronke M., 2022, MNRAS, 510, 551
Farmer A. J., Goldreich P., 2004, ApJ, 604, 671
Ferland G., Korista K., Verner D., Ferguson J., Kingdon J., Verner E., 1998, PASP, 110, 761
Fryxell B. et al., 2000, ApJS, 131, 273
Gentry E. S., Krumholz M. R., Dekel A., Madau P., 2017, MNRAS, 465, 2471
Gentry E. S., Krumholz M. R., Madau P., Lupi A., 2019, MNRAS, 483, 3647
Girichidis P. et al., 2016, ApJ, 816, L19
Girichidis P., Naab T., Hanasz M., Walch S., 2018, MNRAS, 479, 3042
Girichidis P., Naab T., Walch S., Berlok T., 2021, MNRAS, 505, 1083
Gnedin N. Y., Kravtsov A. V., 2011, ApJ, 728, 88
Grenier I. A., Black J. H., Strong A. W., 2015, ARA&A, 53, 199
Gronke M., Oh S. P., 2018, MNRAS, 480, L111
Gronke M., Oh S. P., 2020, MNRAS, 492, 1970
Gunn J. E., Gott J. R. III, 1972, ApJ, 176, 1
Hawley J. F., Balbus S. A., 1999, Phys. Plasmas, 6, 4444
Heintz E., Zweibel E. G., 2018, ApJ, 860, 97
Hernquist L., 1993, ApJS, 86, 389
Holguin F., Ruszkowski M., Lazarian A., Farber R., Yang H. K., 2019, MNRAS, 490, 1271
Hopkins P. F. et al., 2020, MNRAS, 492, 3465
Hopkins P. F., Squire J., Chan T., Quataert E., Ji S., Kereš D., Faucher-Giguère C.-A., 2021, MNRAS, 501, 4184
Huang J., Greengard L., 1999, SIAM J. Sci. Comput., 21, 1551
Hubble E., Humason M. L., 1931, ApJ, 74, 43
Iffrig O., Hennebelle P., 2015, A&A, 576, A95
Ignesti A. et al., 2022, ApJ, 924, 64
Jáchym P., Köppen J., Palouš J., Combes F., 2009, A&A, 500, 693
Jáchym P. et al., 2017, ApJ, 839, 114
Jaffé Y. L., Smith R., Candlish G. N., Poggianti B. M., Sheen Y.-K., Verheijen M. A., 2015, MNRAS, 448, 1715
Ji S. et al., 2020, MNRAS, 496, 4221
Kanjilal V., Dutta A., Sharma P., 2021, MNRAS, 501, 1143
Keller B., Wadsley J., Benincasa S., Couchman H., 2014, MNRAS, 442, 3013
Kennicutt R. C. Jr, 1998, ApJ, 498, 541
Kim C.-G., Ostriker E. C., 2015, ApJ, 802, 99
Kim C.-G., Ostriker E. C., 2017, ApJ, 846, 133
Klein R. I., McKee C. F., Colella P., 1994, ApJ, 420, 213
Kravtsov A., 1999, PhD thesis, New Mexico State Univ.
Kravtsov A. V., Klypin A., Hoffman Y., 2002, ApJ, 571, 563
Kronberger T., Kapferer W., Ferrari C., Unterguggenberger S., Schindler S., 2008, A&A, 481, 337
Krumholz M. R., Tan J. C., 2007, ApJ, 654, 304
Kulsrud R. M., 2005, Plasma Physics for Astrophysics. Princeton Univ. Press, Princeton, NJ
Kulsrud R., Cesarsky C., 1971, ApJ, 8, L189
Kulsrud R., Pearce W. P., 1969, ApJ, 156, 445
Lacki B. C., Thompson T. A., Quataert E., 2010, ApJ, 717, 1
Lazarian A., 2016, ApJ, 833, 131
Lee D., 2013, J. Comput. Phys., 243, 269
Lee D., Deane A. E., 2009, J. Comput. Phys., 228, 952
Lee J., Kimm T., Katz H., Rosdahl J., Devriendt J., Slyz A., 2020, ApJ, 905, 31
Leroy A. K. et al., 2017, ApJ, 846, 71
Li Z., Hopkins P. F., Squire J., Hummels C., 2020, MNRAS, 492, 1841
Lyutikov M., 2006, MNRAS, 373, 73
Mac Low M.-M., McKee C. F., Klein R. I., Stone J. M., Norman M. L., 1994, ApJ, 433, 757
Martizzi D., Faucher-Giguère C.-A., Quataert E., 2015, MNRAS, 450, 504
McKee C. F., Cowie L. L., 1977, ApJ, 215, 213
Miyamoto M., Nagai R., 1975, PASJ, 27, 533
Montero F. R., Martin-Alvarez S., Sijacki D., Slyz A., Devriendt J., Dubois Y., 2022, MNRAS, 511, 1247
Moretti A. et al., 2018, MNRAS, 480, 2508
Moretti A. et al., 2020a, ApJ, 889, 9
Moretti A. et al., 2020b, ApJ, 897, L30
Müller A. et al., 2021, Nat. Astron., 5, 159
Murphy E. J., Kenney J. D. P., Helou G., Chung A., Howell J. H., 2009, ApJ, 694, 1435
Oosterloo T., van Gorkom J., 2005, A&A, 437, L19

Downloaded from https://academic.oup.com/mnras/article/512/4/5927/6553836 by Columbia University user on 10 August 2022

Paladino R., Murgia M., Helfer T. T., Wong T., Ekers R., Blitz L., Gregorini L., Moscadelli L., 2006, A&A, 456, 847
Peluso G. et al., 2022, ApJ, 927, 130
Pfrommer C., Dursi J., 2010, Nat. Phys., 6, 520
Pfrommer C., Pakmor R., Schaal K., Simpson C., Springel V., 2017a, MNRAS, 465, 4500
Pfrommer C., Pakmor R., Simpson C. M., Springel V., 2017b, ApJ, 847, L13
Pittard J. M., 2019, MNRAS, 488, 3376
Poggianti B. M. et al., 2017a, Nature, 548, 304
Poggianti B. M. et al., 2017b, ApJ, 844, 48
Radovich M., Poggianti B., Jaffé Y. L., Moretti A., Bettoni D., Gullieuszik M., Vulcani B., Fritz J., 2019, MNRAS, 486, 486
Ramos-Martínez M., Gómez G. C., Pérez-Villegas Á., 2018, MNRAS, 476, 3781
Ricker P., 2008, ApJS, 176, 293
Roberts I. D., Parker L. C., 2020, MNRAS, 495, 554
Roberts I. et al., 2021, A&A, 650, A111
Roberts I. D., van Weeren R. J., Timmerman R., Botteon A., Gendron-Marsolais M.-L., Ignesti A., Rottgering H. J., 2022, A&A, 658, A44
Roediger E., 2009, Astron. Nachr., 330, 888
Roediger E., Brüggen M., 2006, MNRAS, 369, 567
Roediger E., Brüggen M., Owers M., Ebeling H., Sun M., 2014, MNRAS, 443, L114
Rudd D. H., Zentner A. R., Kravtsov A. V., 2008, ApJ, 672, 19
Ruggiero R., Lima Neto G. B., 2017, MNRAS, 468, 4107
Ruszkowski M., Enßlin T., Brüggen M., Heinz S., Pfrommer C., 2007, MNRAS, 378, 662
Ruszkowski M., Enßlin T., Brüggen M., Begelman M., Churazov E., 2008, MNRAS, 383, 1359
Ruszkowski M., Brüggen M., Lee D., Shin M.-S., 2014, ApJ, 784, 75
Ruszkowski M., Yang H.-Y. K., Zweibel E., 2017, ApJ, 834, 208
Salem M., Bryan G. L., 2014, MNRAS, 437, 3312
Schmidt M., 1959, ApJ, 129, 243
Schulz S., Struck C., 2001, MNRAS, 328, 185
Scodeggio M., Gavazzi G., 1993, ApJ, 409, 110
Semenov V. A., Kravtsov A. V., Gnedin N. Y., 2016, ApJ, 826, 200
Semenov V. A., Kravtsov A. V., Gnedin N. Y., 2017, ApJ, 845, 133
Semenov V. A., Kravtsov A. V., Gnedin N. Y., 2018, ApJ, 861, 4
Semenov V. A., Kravtsov A. V., Caprioli D., 2021, ApJ, 910, 126
Simpson C. M., Pakmor R., Marinacci F., Pfrommer C., Springel V., Glover S. C., Clark P. C., Smith R. J., 2016, ApJ, 827, L29
Sparre M., Pfrommer C., Ehlert K., 2020, MNRAS, 499, 4261
Squire J., Hopkins P. F., Quataert E., Kempski P., 2021, MNRAS, 502, 2630
Steinhauser D., Schindler S., Springel V., 2016, A&A, 591, A51
Stone J. M., Norman M. L., 1992, ApJS, 80, 753
Su M., Slatyer T. R., Finkbeiner D. P., 2010, ApJ, 724, 1044
Sun M., Jones C., Forman W., Nulsen P., Donahue M., Voit G., 2006, ApJ, 637, L81
Sun M., Donahue M., Roediger E., Nulsen P., Voit G., Sarazin C., Forman W., Jones C., 2009, ApJ, 708, 946
Tonnesen S., 2019, ApJ, 874, 161
Tonnesen S., Bryan G. L., 2009, ApJ, 694, 789
Tonnesen S., Bryan G. L., 2010, ApJ, 709, 1203
Tonnesen S., Bryan G. L., 2012, MNRAS, 422, 1609
Tonnesen S., Bryan G. L., 2021, ApJ, 911, 68
Tonnesen S., Stone J., 2014, ApJ, 795, 148
Trachternach C., De Blok W., Walter F., Brinks E., Kennicutt R. Jr, 2008, AJ, 136, 2720
Trapp C. W. et al., 2022, MNRAS, 509, 4149
Turk M. J., Smith B. D., Oishi J. S., Skory S., Skillman S. W., Abel T., Norman M. L., 2010, ApJS, 192, 9
Uhlig M., Pfrommer C., Sharma M., Nath B. B., Enßlin T., Springel V., 2012, MNRAS, 423, 2374
Vollmer B., Soida M., Chung A., Chemin L., Braine J., Boselli A., Beck R., 2009, A&A, 496, 669
Vollmer B., Soida M., Chung A., Beck R., Urbanik M., Chyzy K. T., Otmianowska-Mazur K., Gorkom J. H. V., 2010, A&A, 512, A36
Vollmer B., Soida M., Beck R., Chung A., Urbanik M., Chyzy K. T., Otmianowska-Mazur K., Kenney J. D. P., 2013, A&A, 553, A116
Vulcani B. et al., 2018, ApJ, 866, L25
Walch S., Naab T., 2015, MNRAS, 451, 2757
Werk J. K., Prochaska J. X., Thom C., Tumlinson J., Tripp T. M., O'Meara J. M., Peeples M. S., 2013, ApJS, 204, 17
Wiener J., Pfrommer C., Oh S. P., 2017, MNRAS, 467, 906
Wiener J., Zweibel E. G., Oh S. P., 2018, MNRAS, 473, 3095
Wiener J., Zweibel E. G., Ruszkowski M., 2019, MNRAS, 489, 205
Xu J., Stone J. M., 1995, ApJ, 454, 172
Yang H.-Y., Ruszkowski M., 2017, ApJ, 850, 2
Yang H.-Y., Ruszkowski M., Ricker P., Zweibel E., Lee D., 2012, ApJ, 761, 185
Yang H.-Y. K., Ruszkowski M., Zweibel E., 2013, MNRAS, 436, 2734
Yun M. S., Reddy N. A., Condon J. J., 2001, ApJ, 554, 803
Zhang B. et al., 2013, ApJ, 777, 122
Zweibel E. G., 2017, Phys. Plasmas, 24, 055402
Zweibel E. G., 2020, ApJ, 890, 67

APPENDIX A: CONVERGENCE

Due to computational expense, we are somewhat limited in physical resolution ∼127 pc in the runs presented above. We expect the accretion rate towards the centre of the galaxy to be unresolved and hence we caution interpretation of the central regions of Fig. 8 with a grey region.

Although the expense was rather large, we managed to perform simulations of the DIF runs at ∼63 pc resolution to test convergence. We find rather good agreement in the star formation history across resolution, as shown in Fig. A1.

Importantly, the results are qualitatively the same: EdgeOn boosts SFRs more than FaceOn stripping. In detail, however, the FaceOn-DIF run at higher resolution attains a stronger burst at > 175 Myr, whereas the Isolated-DIF run at higher resolution exhibits lower SFR. The combined effect is a boost in star formation due to RPS beyond the observed range. However, we had similarly disfavoured the FaceOn-DIF run based on the accretion rate plot. That is, in Section 3.5 we found that CRs suppress accretion towards the galactic centre, whereas observations detect a higher AGN fraction in ram-pressure-stripped galaxies (Poggianti et al. 2017a; Radovich et al. 2019; Peluso et al. 2022), suggesting enhanced accretion towards the galactic centre. Thus, our end results are not impacted, even if the details are a bit different.

Nevertheless, the SFR is quite similar in comparing the fiducial and high-resolution runs for most of the simulated time for most

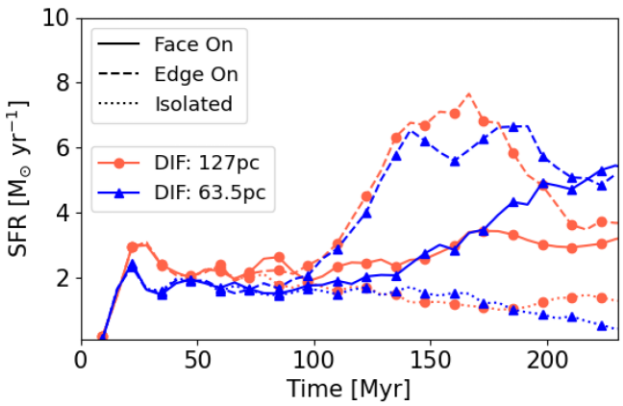

Figure A1. Time series of SFR for the `FaceOn` (solid), `EdgeOn` (dashed), and `Isolated` (dotted) DIF runs comparing our fiducial 127 pc resolution (red circles) to a set of high 63.5 pc resolution (blue triangles) runs. Overall, we find good agreement between the fiducial and high-resolution runs.

Downloaded from https://academic.oup.com/mnras/article/512/4/5927/6553836 by Columbia University user on 10 August 2022

of the physics and wind cases. This is rather surprising as high-resolution ISM slab simulations suggest SFRs do not converge until ∼8 pc resolution (Kim & Ostriker 2017).

APPENDIX B: TRUE DIODE BOUNDARY CONDITIONS

Diode boundary conditions allow material to flow out of the computational domain but are intended to prevent inflow. In FLASH, boundary conditions apply conditions to *cell-centred* values of ghost cells which border the physical computational domain. The default diode boundary condition implementation in FLASH simply replaces the velocity component normal to the boundary with zero when it is negative. However, since the Riemann problem solves for the fluxes at cell *interfaces* to update hydrodynamic terms, even if the ghost cell-centred velocity is zero, an inflowing velocity at the ultimate interior cell (UIC) will result in an inflow across the interface. This problem generically leads to non-conservation of mass when gravitational acceleration is present (as well as similar acceleration profiles).

Therefore, we apply the diode condition to the UIC cells, guaranteeing the flux across the physical domain boundary does not permit inflows. This simple, yet effective modification ensured conservation of mass. In our test, we initialized an 8^3 box with a static gas of uniform temperature 7×10^7 K and density 10^{-27} g cm^{-3}. We turned off magnetic fields, cooling and heating, and star formation and feedback. However, we maintained the static potentials described in Section 2.1. In Fig. B1, we show default (corrected) diode boundary conditions with solid blue (red dashed) curves, with the corrected diode boundary conditions indicating marked improvement.

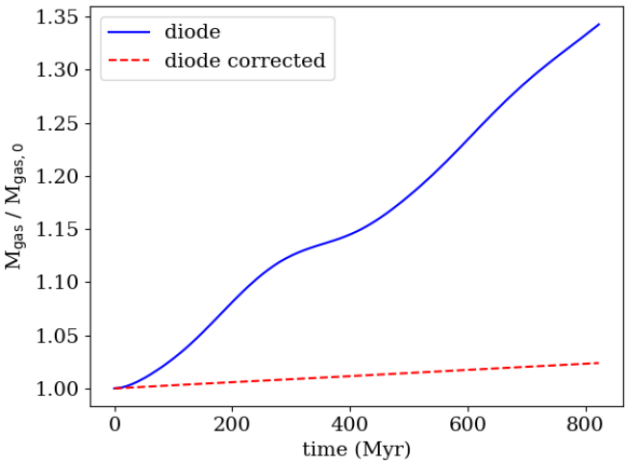

Figure B1. Conservation of mass with time. The solid blue (dashed red) curves indicate the default (corrected) diode boundary conditions. The corrected diode boundary conditions show marked improvement in mass conservation.

We note that with large box sizes and higher resolution such that the acceleration at the UIC vanishes, non-conservation of mass also vanishes. Related to computational constraints, we were unable to perform our fiducial simulations in larger box sizes (except at lower resolution).

This paper has been typeset from a TEX/LATEX file prepared by the author.

Downloaded from https://academic.oup.com/mnras/article/512/4/5927/6553836 by Columbia University user on 10 August 2022